

Magnetic Resonance Imaging of Gas–Solid Fluidization with Liquid Bridging

C. M. Boyce *

Dept. of Chemical Engineering, Columbia University, New York, NY, USA

Dept. of Mechanical and Process Engineering, ETH Zurich, Zurich, Switzerland

A. Penn*

Dept. of Mechanical and Process Engineering, ETH Zurich, Zurich, Switzerland

Institute for Biomedical Engineering, ETH Zurich and University of Zurich, Zurich, Switzerland

K. P. Pruessmann

Institute for Biomedical Engineering, ETH Zurich and University of Zurich

C. R. Müller

Dept. of Mechanical and Process Engineering, ETH Zurich

DOI 10.1002/aic.16036

Published online December 5, 2017 in Wiley Online Library (wileyonlinelibrary.com)

*Magnetic resonance imaging is used to generate snapshots of particle concentration and velocity fields in gas–solid fluidized beds into which small amounts of liquid are injected. Three regimes of bed behavior (stationary, channeling, and bubbling) are mapped based on superficial velocity and liquid loading. Images are analyzed to determine quantitatively the number of bubbles, the bubble diameter, bed height, and the distribution of particle speeds under different wetting conditions. The cohesion and dissipation provided by liquid bridges cause an increase in the minimum fluidization velocity and a decrease in the number of bubbles and fast particles in the bed. Changes in liquid loading alter hydrodynamics to a greater extent than changes in surface tension or viscosity. Keeping U/U_{mf} at a constant value of 1.5 produced fairly similar hydrodynamics across different wetting conditions. The detailed results presented provide an important dataset for assessment of the validity of assumptions in computational models. © 2017 American Institute of Chemical Engineers *AIChE J*, 64: 2958–2971, 2018*

Keywords: fluidization, liquid bridging, magnetic resonance imaging

Introduction

In industries including pharmaceutical, energy, and food production, small amounts (~ 1 wt %) of liquid are injected into gas–solid fluidized beds in order to facilitate chemical reactions or the agglomeration of particles. This injection leads to the formation of liquid bridges between particles which create viscous and capillary forces between the particles altering the particle-scale and device-scale hydrodynamics. This process, often referred to as “wet fluidization,” has been the subject of many experimental and modeling studies, due to its industrial relevance and the scientifically interesting effects of liquid bridging on fluidized bed behavior.

On a smaller scale, the cohesion between particles and the dissipation of relative motion between particles due to liquid

bridges causes particles to agglomerate. On a larger scale, this leads to greater heterogeneity in gas and particle flow, affecting many aspects of fluidization hydrodynamics, which in turn alters heat and mass transport as well as chemical reactions. Previous studies have shown that the addition of small amounts of liquid alters the oscillations in pressure drop across the bed,^{1,2} slows the speed of particles,^{2–4} and increases the minimum fluidization velocity.^{5–7} Studies have also sought to map the behavior of wet fluidized beds into regimes based on the amount of liquid added as well as the surface tension and viscosity of the liquid; these regimes have included shifts in the Geldart⁸ grouping of the particles^{6,7,9} and the growth or breakup of agglomerates.^{10–13} Despite decades of studies, key questions remain open in the field, including the relative importance of liquid loading, surface tension, and viscosity of the liquid,^{5,10,14} the non-dimensionalization of liquid bridge behavior based on force- or energy-based analyses^{5,10,12} and the validity of approximating a wet and dry bed of behaving similarly if the ratio of superficial velocity to minimum fluidization velocity (U/U_{mf}) is kept constant.⁵ Boyce¹⁵ provides a review of prior work in wet fluidization, highlighting open questions and areas for future work.

Additional Supporting Information may be found in the online version of this article.

*These authors contributed equally to the work.

Correspondence concerning this article should be addressed to C. M. Boyce at cmb2302@columbia.edu.

Difficulties in fully understanding the effects of liquid bridging on fluidization hydrodynamics stem in part from a lack of temporally and spatially resolved experimental data on gas and particle motion in wet fluidized beds. Previous studies have been limited to device-scale measurements, such as pressure oscillations^{1,2} and fluidization curves,^{5,6} measurements on pseudo-2D fluidized beds using optical imaging^{2,4} and tomographic measurements on 3D beds of tracer particles,³ which are unable to capture behavior across the entire device on a temporally resolved level. In recent years, magnetic resonance imaging (MRI) has been able to generate detailed maps of both particle^{16–21} and gas^{18,22–24} motion in fluidized beds. A recent study¹⁹ using a medical MRI scanner and multichannel signal detection has enabled millisecond-scale temporal resolution of maps of particle concentration and velocity in 3D beds with a diameter and height of over 100 particle diameters. In this article, we apply this MRI technique, alongside traditional fluidization curves, to study the effects of liquid loading and liquid properties on fluidization hydrodynamics. We use these detailed insights to provide a regime map of bed behavior based on U/U_{mf} and liquid loading, as well as analysis of the effects of liquid bridging on bubble size, the number of bubbles, bed height, and particle speed.

Experimental

Fluidized bed

A fluidized bed was constructed from polymethyl methacrylate (PMMA) with an inner diameter of 190 mm and a height of 300 mm. The distributor was made from a PMMA plate drilled with 0.5 mm holes and even gas distribution was confirmed by taking MR images of horizontal slices through the bed and noting that bubbles formed at approximately equal frequencies throughout all regions of the bed. The bed was filled with brown mustard seeds sieved to a size range of 1.4–1.6 mm to a height of 146 mm, corresponding to a weight of 3.00 kg. Digital imaging and image analysis of ~ 1000 sieved particles showed that the average particle diameter was $d_p = 1.50$ mm with a standard deviation in the particle size distribution of 0.09 mm. The particles had a density of 1080 kg/m³. The bed was fluidized with air at ambient conditions.

Liquid addition

Liquid was sprayed into the top of the bed in between measurements using spray bottles in increments of 6 g, corresponding to 0.2 wt %. After spraying, the bed was vigorously fluidized and shaken for several minutes to ensure even distribution of liquid on the surfaces of particles. Silicone oils and benzyl benzoate were chosen due to their low vapor pressures and hydrophobicity, such that they did not evaporate and were not absorbed by the particles during the experiment. Silicone oil was used as obtained from Paragon Scientific. Two silicone oils were used: (1) with a viscosity of 5 mPa s, a surface tension of 20 mN/m, and a density of 910 kg/m³ and (2) with a viscosity of 100 mPa s, a surface tension of 20 mN/m and a density of 990 kg/m³. Benzyl benzoate was used as obtained from Fischer Scientific with a viscosity of 8 mPa s, a surface tension of 40 mN/m, and a density of 1120 kg/m³.

It is worth noting that McDougall et al.¹³ studied the effects of liquid on agglomeration behavior across a wide range of three-phase contact angles, finding a major shift in behavior at a contact angle of approximately 40°. Since our facilities were not capable of measuring contact angle on powders via the

Washburn method²⁵ or atomic force microscope techniques,²⁶ we estimated the contact angle using simple techniques. Upon placing a single particle on a thin film of liquid and taking high-resolution photographs, it was found that all three liquids used enveloped the particle, coming into contact with the particle surface at a low contact angle, close to zero. Since this is very far from the critical value of 40° found by McDougall et al.,¹³ we conclude that contact angle was not an important differentiator between the liquids used.

Fluidization curves

Fluidization curves were obtained by inserting a pressure probe into the bed, just above the distributor. The superficial gas velocity (U) was slowly decreased from a bubbling fluidization state to $U = 0$ m/s while the pressure drop across the bed was recorded in order to obtain the fluidization curve for decreasing U . Directly after this measurement, U was slowly increased until a bubbling fluidization state was reached in order to obtain an increasing U curve. Two sets of fluidization curves were collected before MRI experiments and one set was obtained after, in order to ensure consistency in bed behavior over time.

The minimum fluidization velocity (U_{mf}) and the full fluidization velocity (U_{ff}) were determined based on the decreasing U curve. U_{mf} was evaluated by creating a linear regression through the data points with a pressure drop normalized by the weight of the bed per unit area between 0.5 and 0.75. This linear regression was extrapolated to the point at which the normalized pressure drop equaled 1.0, and the value of U at this point was used as U_{mf} . The full fluidization velocity was determined based on the lowest value of U at which the pressure drop normalized by the weight of the bed per unit cross-sectional area was equal to 0.98 or greater. U_{mf} and U_{ff} differed in many cases due to the non-linear behavior of the curves for normalized pressure drops above 0.75.

Due to cohesion-induced hysteresis in the system, the increasing U and decreasing U curves differed in several cases. In order to quantify this difference, a pseudo minimum fluidization velocity, $U_{mf,up}$, was calculated using the same linear regression and extrapolation method for the increasing U curve.

Magnetic resonance imaging

Magnetic resonance imaging experiments were conducted in a Phillips Achieva 3T medical MRI scanner. Signal excitation was conducted with the body radiofrequency (r.f.) coil of the medical scanner, while signal detection was conducted using a custom-built 16-channel coil which fit directly around the fluidized bed.¹⁹ Magnetic resonance (MR) signal was received from the oil within the mustard seeds, enabling imaging of the particles. Echo planar imaging (EPI)²⁷ was used to enable snapshot imaging with a single excitation pulse. As detailed by Penn et al.,¹⁹ partial sampling of frequency space based on Hermitian symmetry and sampling below the Nyquist limit²⁸ enabled by multichannel signal reception and SENSE²⁹ reconstruction were used to enable snapshot imaging with increased temporal resolution. Images were obtained in a slice through a vertical cross-section of the bed. Images of both particle distribution and particle velocity were obtained using standard EPI and phase-contrast³⁰ EPI, respectively.

For the standard EPI measurements, the spatial resolution was 3 mm (horizontal) \times 3 mm (vertical) with a 10 mm slice in the third direction. As shown in the previous study,¹⁹ the

standard EPI measurements allow for images to be obtained at rates up to 150 Hz, allowing the evolution of individual bubbles over time to be tracked. However, for these specific measurements, we were more concerned with obtaining high quality images of bubbles for statistical analysis and less concerned with the time between successive images. Thus, to obtain a higher signal-to-noise ratio while still capturing dynamic snapshots, the standard EPI measurements were run with an echo time of 1.30 ms and an acquisition time of 6 ms, but a repetition time between excitations of 200 ms and a flip angle of 63°.

In contrast to the spin density measurements, the phase-contrast EPI measurements were run in such a way to obtain dynamic snapshots at a higher frequency with a lower signal-to-noise ratio. The phase-contrast method³¹ measures velocity based on the phase of magnetic resonance signal, rather than intensity. When two bipolar flow-encoding gradients are used in a measurement, the difference in the phase of the measured signal as compared to that from a measurement without flow-encoding gradients is proportional to the displacement of particles in between flow-encoding gradients. Assuming the velocity of the particles is uniform across the short time interval between flow-encoding gradients, the velocity is determined as the displacement divided by the time interval. This phase-contrast method can be combined with imaging to generate maps of particle velocity. In the experiments run in this study, three excitations were used per image, one without phase encoding, one with phase encoding in the horizontal direction and one with phase encoding in the vertical direction, so as to generate snapshot maps of the in-plane velocity field. The phase-contrast EPI pulse sequence had an echo time of 1.86 ms, a repetition time of 6.7 ms, and a temporal resolution of 20 ms in between successive velocity field images. The spatial resolution of the phase contrast EPI images was 3 mm (horizontal) × 5 mm (vertical) with a 15 mm slice in the third direction. A flip angle of 15° was used.

It is worth noting that the added liquid will also provide MRI signal, in addition to that coming from the oil in the particles. However, the mustard seeds consist of ~40 wt % oil,¹⁹ and thus the addition of ~1 wt % liquid will not have a significant influence on the signal. Further, since the oil is uniformly distributed on the surfaces of particles, it would only slightly enhance the signal from particles, which would not corrupt the data on bubble behavior or particle motion in any way.

The specified spatial resolutions of the acquisitions refer to the nominal resolution that results from the maximum acquired k -space values k_x^{max} according to the Fourier relation $\Delta x = \frac{2\pi}{k_x^{max}}$. However, there are multiple factors that can have an effect on the true spatial resolution of an MRI measurement, such as sample motion, limited signal lifetime and chemical shift effects. While chemical shift effects play a negligible role in this study, the signal lifetime of the mustard seeds limits the spatial resolution in the vertical (phase encoding) direction. In order to identify the threshold above which a further enhancement of the nominal spatial resolution has no effect on the produced image, we varied the nominal spatial resolution and evaluated the effect on the image qualitatively. The chosen spatial resolution of 3 mm × 3 mm is within this cutoff. The strongest influence on the true spatial resolution has, however, sample motion. The speed of the particles v_p , and the duration of the acquisition T_{acq} set the upper bound for the true spatial resolution in the direction of motion to $\Delta x \geq v_p/T_{acq}$. For particles that move at a speed of 0.5 m/s

this upper bound corresponds to one unit of the nominal spatial resolution for particle density measurement. For particle velocity measurements, however, the value is slightly more than three times larger.

Image processing

Magnetic resonance imaging data was processed in MATLAB using the MRecon interface (ReconFrame 3.0, GyroTools LLC, Zurich, Switzerland). In order to obtain data on bubbles, a threshold was applied to the images. Pixels with a signal intensity greater than 17% of the signal intensity from the pixel with the maximum signal intensity in the image series were considered as consisting of the particle-laden phase. Pixels with a signal intensity lower than this threshold value were considered as consisting of the gas phase, either being part of a bubble or the freeboard of the bed. The validity of this threshold value was confirmed by visually matching raw images and thresholded images as well as confirming that bubble data did not change significantly when the threshold value was changed by 5% in either direction.

For bubble analysis, interconnected pixels of the gas phase were registered as a single bubble. An equivalent bubble diameter was calculated for each bubble based on the diameter of a circle with the same area as that of the bubble. The centroid point of each bubble was evaluated in order to bin bubble data based on the vertical distance of the bubble center above the distributor, i.e., the “height” of the bubble in the bed. The number of bubbles recorded in the 500 images obtained was also analyzed in order to compare data on the number of bubbles in the system across experimental conditions.

The same threshold-based procedure was used to analyze the expanded bed height in each image. The expanded bed height was taken as the highest point in the contiguous region of the particle-laden phase; thus, this height did not account for small particle laden regions sent into the freeboard due to bubble eruption. The mean value and standard deviation of the values of standard bed height in the time series of images were evaluated for comparison across various wetting and gas flow rate conditions.

To analyze the extent to which a bed was vigorously fluidized, involving rapid changes between bubbles and particles occupying a pixel, the collective standard deviation in MRI signal intensity was evaluated:

$$\sigma_S = \sqrt{\frac{\sum_{t=1}^{N_{times}} \sum_{i=1}^{N_{pixels}} (S_i(t) - S_{i,avg})^2}{N_{times}}} - \sqrt{\frac{\sum_{t=1}^{N_{times}} \sum_{i=1}^{N_{pixels}} (S_{i,stationary} - S_{i,stationary,avg})^2}{N_{times}}} \quad (1)$$

Where N_{times} is the number of snapshot images, N_{pixels} is the number of pixels in each image, $S_i(t)$ is the signal in pixel i at time t , and $S_{i,avg}$ is the signal in pixel i averaged over time. In this equation, the second term on the right hand side is equivalent to the first, but for a stationary bed, so as to subtract off the difference in signal in pixels over time due to noise, but still account for the difference in signal over time due to the motion of voids through the system. Thus, σ_S produces a value of 0 if the bed is stationary and a high value if the bed is vigorously fluidized, with pixels constantly changing from having a

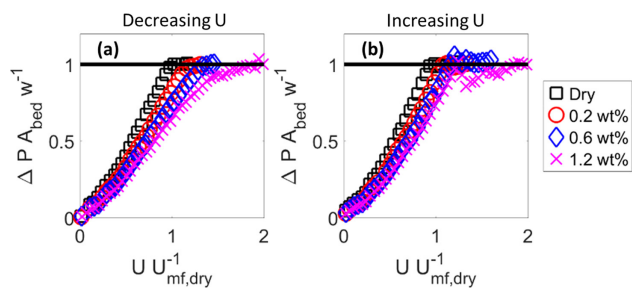


Figure 1. Fluidization curves (a) decreasing U and (b) increasing U for cases with different amounts of 5 mPa s silicone oil.

[Color figure can be viewed at wileyonlinelibrary.com]

high MRI signal to a low signal due to the motion of particles and bubbles in the system.

The same 17% threshold based on signal intensity was also applied to images of in-plane particle speed in order to obtain particle speeds from pixels containing the particle-laden phase. The speed from these particle-containing pixels was recorded over the 1000 images taken for each experimental condition in order to give a distribution of in-plane particle speeds.

Results

The results of this article are summarized in a Supporting Information Video and all data used to create images, videos, and figures in the article are provided on Prof. Christoph Müller's website in the form of text and Matlab files, with relevant Matlab scripts for processing the data.

Fluidization curves

Figure 1 shows fluidization curves with varying content of 5 mPa s silicone oil for (a) decreasing U and (b) increasing U . On the vertical axis, the pressure drop across the bed is normalized by the weight of the bed per unit area, such that a value of 1.0 indicates that the gas flow is sufficient to suspend the particles. On the horizontal axis, the superficial velocity is normalized by the minimum fluidization velocity for the dry case. The decreasing and increasing U curves for the dry case are nearly identical with normalized pressure drop increasing linearly with U from a normalized pressure drop of 0.3–1.0 before leveling off at 1.0 when $U/U_{mf,dry} = 1.0$.

The curves with liquid loadings of 0.2 and 0.6 wt % look similar to those for the dry case, but with the curves shifted to the right, i.e., having a higher value of U to achieve the same

value of normalized pressure drop. This shift to the right indicates an increase in U_{mf} . A recent computational study⁵ has linked this increase in U_{mf} to decreasing packing density and homogeneity in the packing with increasing cohesion due to liquid in the bed. For increasing U , the curves also shift to the right, but to a lesser extent as compared to the decreasing curves. This difference in the shift to the right can be attributed to the fact that particles are locked in place in the increasing U curve until a normalized pressure drop of 1 is reached, keeping their structure more homogeneous and dense than in the decreasing U case.

For the decreasing U curve with a liquid loading of 1.2 wt %, a strong shift to the right is observed, especially at values of normalized pressure drop between 0.9 and 1.0. For the corresponding increasing U curve, a normalized pressure drop of 1 is first reached at $U/U_{mf,dry} \sim 1.1$; however at higher values of U , the normalized pressure drop decreases to values below 1 until it levels off at a value of 1 at $U/U_{mf,dry} \sim 1.8$. This behavior is attributed to the gas velocity becoming sufficient to jar the particles out of their initial configuration at $U/U_{mf,dry} = 1.1$, but the gas then channeling through selected void regions rather than fully fluidizing the bed. At $U/U_{mf,dry} = 1.8$, the gas flow is finally capable of fully supporting the weight of the bed in a bubbling fluidization state. The increase in U_{mf} seen with liquid loading and the increase in difference between increasing U and decreasing U curves with the addition of liquid are consistent with findings from previous experimental^{6,7} and computational⁵ studies.

Figure 2a shows U_{mf} for wet cases normalized by that for the dry case vs. liquid loading for three different liquids. In all cases, U_{mf} increases monotonically with liquid loading. For values of liquid loading below 0.8 wt %, U_{mf} increases slightly with increasing viscosity and surface tension, consistent with the assertion that increasing cohesion provides the origin for increasing U_{mf} . At values of liquid loading above 0.8 wt %, U_{mf} is essentially independent of liquid viscosity. Measurements of high surface tension liquid at higher values of liquid loading were unable to be conducted due to damage to PMMA caused by benzyl benzoate.

Figure 2b shows that for all wet and dry cases, the value of U_{mf} evaluated based on the decreasing U curve was greater than the value $U_{mf,up}$ evaluated based on the increasing U curve. This difference is explained by the locking mechanism described previously in this section. Figure 2b shows that the ratio between the two values increases with increasing liquid loading and to a lesser extent with increasing surface tension and viscosity. This increase can be attributed to a greater

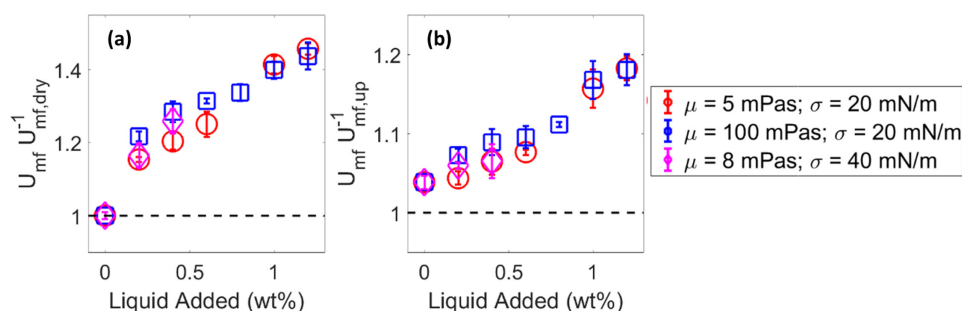


Figure 2. Ratio of (a) minimum fluidization velocity to that of a dry bed and (b) minimum fluidization velocity to minimum fluidization velocity for a curve with increasing U vs. liquid loading for various liquids.

Error bars show the standard deviation over three measurements. [Color figure can be viewed at wileyonlinelibrary.com]

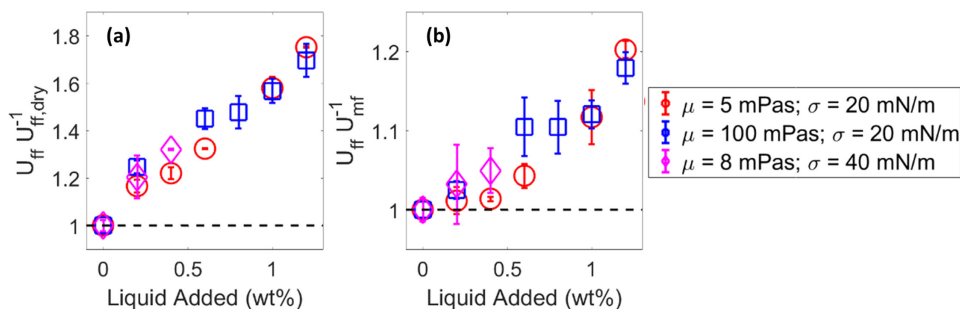


Figure 3. Ratio of (a) full fluidization velocity to that of a dry bed and (b) full fluidization velocity to minimum fluidization velocity vs. liquid loading for various liquids.

Error bars show the standard deviation over three measurements. [Color figure can be viewed at wileyonlinelibrary.com]

difference in the density and homogeneity of the packing at U_{mf} and $U_{mf,up}$ with increasing cohesion in the system due to liquid bridging.

Figure 3a shows the full fluidization velocity for wet cases normalized by that of the dry case for the three liquids as a function of liquid loading. Similar to U_{mf} , U_{ff} increases monotonically with liquid loading for all liquids. Also similar to U_{mf} , U_{ff} increases slightly at low values of liquid loading with increasing viscosity and surface tension; however, U_{ff} is almost independent of viscosity at higher values of liquid loading. Figure 3b shows the ratio of U_{ff} to U_{mf} for both wet and dry cases. For the dry case, U_{mf} and U_{ff} are nearly identical; however, for wet cases the ratio is always greater than 1 and increases monotonically with liquid loading. This increase in U_{ff} relative to U_{mf} with liquid loading indicates that increased cohesion leads to an increased range of gas flow rates at which channeling and partial fluidization are observed with increased cohesion due to liquid bridging.

Regime mapping

From analyzing 500 particle distribution images produced by MRI measurements for each liquid loading condition, the bed behavior was divided into three regimes: (1) Stationary, indicating that particles were not moving at all in the bed. (2) Channeling, indicating that bubbles channeled through small regions of the bed, leaving particles stationary in most regions of the bed. (3) Bubbling, indicating that the entire bed was undergoing bubbling fluidization with particles moving in all regions. Figure 4 shows example images of these three states; the Supporting Information Video provides a time series of images for the three states.

Figure 5 provides a regime map for fluidized bed behavior based on superficial gas velocity and liquid loading for each of

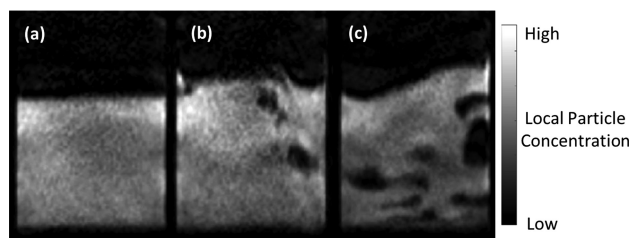


Figure 4. MRI maps of local particle concentration indicative of three regimes for bed behavior: (a) stationary bed, (b) channeling bed, and (c) bubbling fluidized bed.

the three liquids tested. With only a few exceptions, all three liquids produced the same bed behavior for the same liquid loading and gas velocity. Bubbling fluidization occurred for experimental conditions with low liquid loading and high gas velocity, since the gas velocity was able to overcome the agglomeration of particles and fluidize them in these cases. In contrast, with low gas velocity and high liquid loading, the bed became stationary as cohesion between particles caused them to behave as several large agglomerates or one large plug, which low gas flow rates were unable to suspend. For medium and high levels of liquid loading and intermediate gas flow rates, the channeling regime is observed because gas flow is sufficient to breakup certain agglomerated regions so that voids can travel through them, but insufficient to break up all of these regions and support the full weight of the bed.

This map based on MRI measurements is consistent with results from the fluidization curves. Increasing U_{mf} with

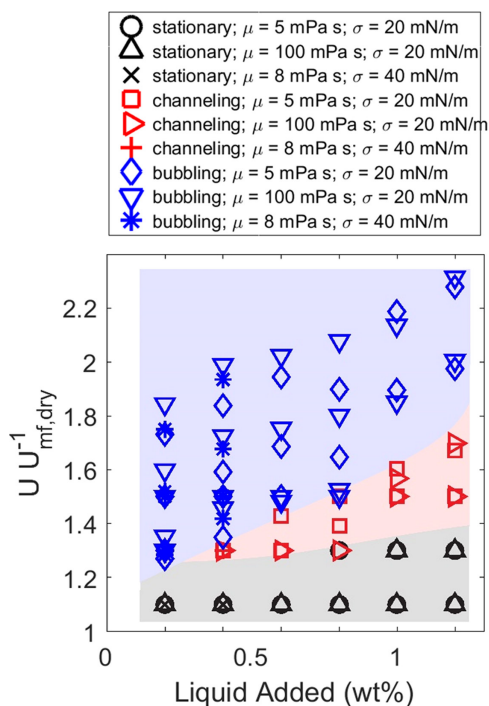


Figure 5. Regime map for fluidized bed behavior based on liquid loading and superficial gas velocity (U) for various liquids.

[Color figure can be viewed at wileyonlinelibrary.com]

increasing liquid loading corresponds to the increased gas velocity necessary to transition out of the stationary regime with increasing liquid loading. Increasing U_{ff} with increased liquid loading corresponds to the increased gas velocity needed to achieve bubbling fluidization with increasing liquid loading.

Bed hydrodynamics

Magnetic resonance imaging allowed for much more detailed insights into the effect of liquid bridging on fluidization hydrodynamics than provided by fluidization curves and regime mapping in the previous sections. Figure 6 shows a comparison of the bed hydrodynamics for (a) a dry case and (b) a wet case with 0.8 wt % 5 mPa s silicone oil. The comparison shows the particle distribution (top row) and particle velocity (bottom row) in a central vertical slice through the bed. Successive images show the evolution of the bed behavior over time. For both cases, the gas velocity was set to $1.5 U/U_{mf,dry}$. In Figure 6a, the top row shows the particle distribution, revealing many bubbles in this vigorously fluidized bed, including two bubbles which start near the center of the bed and grow as they rise to the top of the bed and breakthrough the bed surface. The second row shows the corresponding

particle velocity field as measured using MRI with colors indicating in-plane particle speed and arrows indicating direction. Fast particle speeds up to 1 m/s are observed near bubbles, while slower speeds are seen in other regions of the bed.

Figure 6b shows the corresponding particle distribution and speed images for a wet bed. For an appropriate comparison, we observe a bubble start at the center of the bed and grow and rise to the top of the bed. In this case, only one or two bubbles are seen in the bed at any instance in time. As in the dry case, the fastest particle speeds are seen in regions surrounding bubbles, yet these speeds are considerably lower. Most regions of the bed have particle speeds below 0.1 m/s. These results show qualitatively how cohesion due to liquid bridging makes it more difficult for bubbles to rise freely through beds, as it becomes more difficult to move particles relative to one another due to viscous and capillary forces. The decrease in speed of particles is consistent with previous studies in pseudo-2D beds,^{2,4} a study using particle tracking to find average particle speed on a temporally unresolved level³ and a computational study of a 3D bed.⁵ The Supporting Information Video shows a set of videos of fluidization behavior for these dry and wet cases with values of $U/U_{mf,dry}$ and $U/U_{mf,wet}$ of 1.1, 1.3, and 1.5 to provide a fuller comparison.

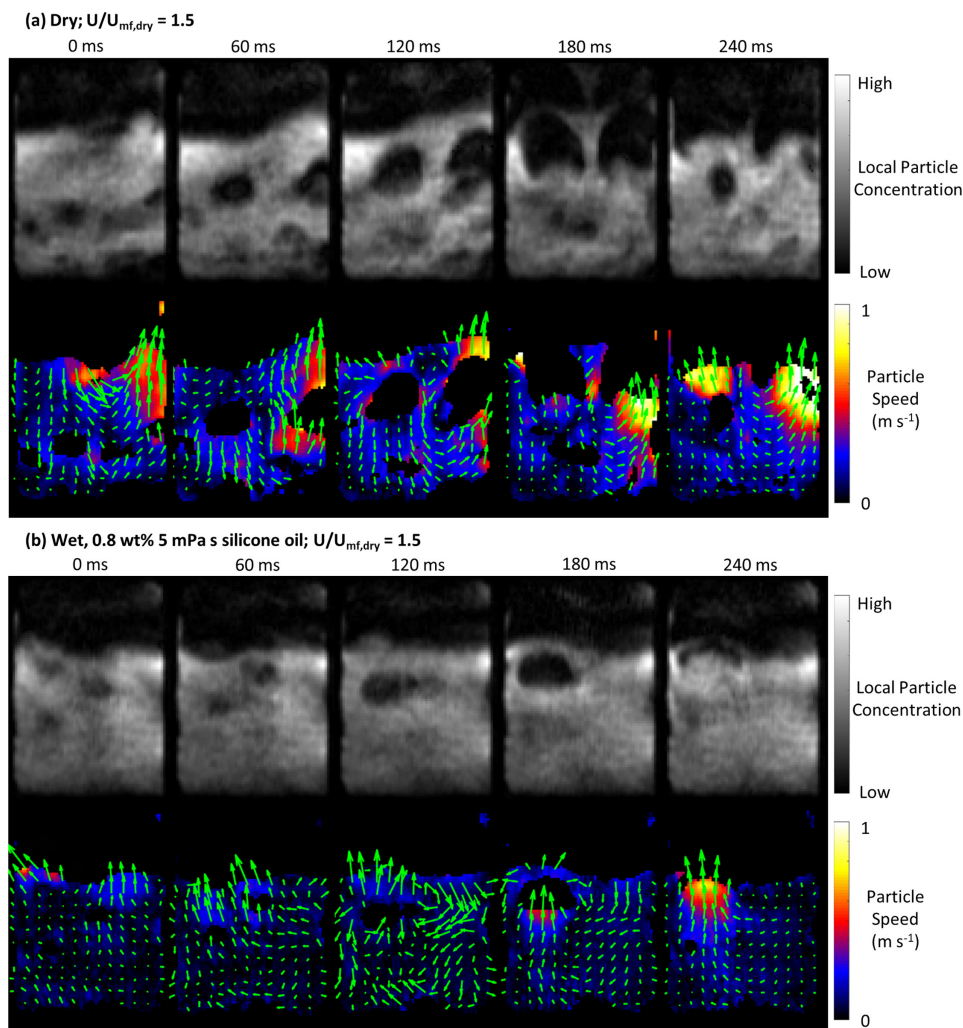


Figure 6. MRI maps of local particle concentration (top row) and local particle velocity (bottom row) over time from a central slice of the fluidized bed for (a) a dry bed and (b) a wet bed with 0.8 wt % of 5 mPa s silicone oil.

[Color figure can be viewed at wileyonlinelibrary.com]

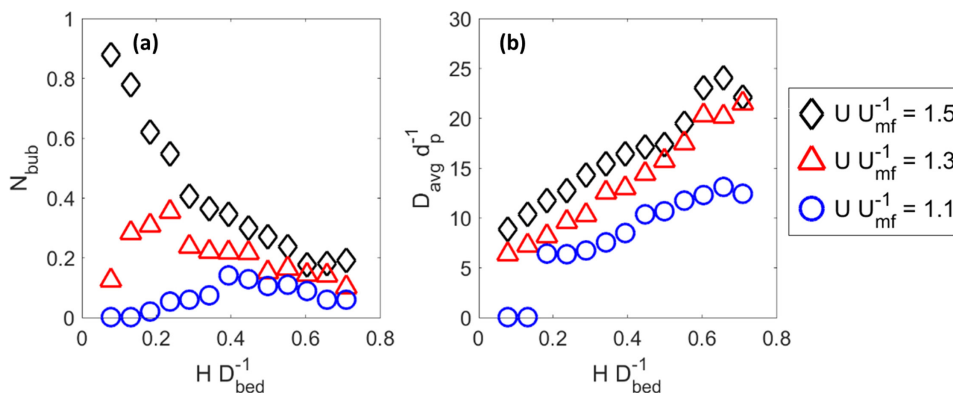


Figure 7. (a) Average number of bubbles per frame and (b) average bubble diameter vs. vertical height in the bed normalized by bed diameter based on threshold analysis of MRI data.

[Color figure can be viewed at wileyonlinelibrary.com]

In order to quantify the effects shown in Figure 6 and the Supporting Information Video, the average number of bubbles, average bubble diameter and distribution of particle speeds were determined for each experimental condition based on thresholding analysis of hundreds of images. Figure 7 shows (a) the average number of bubbles per image and (b) the average bubble diameter observed for a dry fluidized bed at different flow rates as a function of the height of the bubbles in the bed. The number of bubbles increases at all heights with increasing gas velocity, which can be explained by a greater amount of gas flowing through the bed in the form of bubbles at increased flow rates according to the two-phase theory of fluidization.³² For $U/U_{mf,dry} = 1.5$, the number of bubbles decreases monotonically with increasing height in the bed because bubbles coalesce as they rise through the bed. For lower values of U , the number of bubbles increases with increasing height low in the bed and then decreases with increasing height higher in the bed. This behavior can be attributed to the fact that only bubbles with an effective diameter of 6 mm and higher were registered as real bubbles in the post-processing, and thus smaller bubbles in these lower velocity cases had to coalesce before they were observed in this bubble count.

The average bubble diameter at different heights in the dry bed is shown in Figure 7b. The bubble diameter increases monotonically with bed height due to bubbles coalescing as well as potentially absorbing air from surrounding interstices as they rise through the bed. The bubble diameter also increases monotonically with gas flow rate at each height in

the bed due to more gas going into bubbles at higher flow rates. The same patterns with regards to bed height were seen for wet cases; for simplicity of comparison, only data averaged over the entire vertical cross-section of the bed is presented in the remainder of the article.

Figure 8 shows the average number of bubbles per image vs. gas flow rate for the dry case as well as three different liquid cases, each with a liquid loading of 0.2 wt %. Figure 8a gives the results for cases in which $U/U_{mf,dry}$ is specified while (b) gives results for cases in which $U/U_{mf,wet}$ is specified. Thus, for the results in Figure 8 (a), the gas flow rate U is the same for data points with the same value on the horizontal axis. However, for the results in Figure 8b, the gas flow rate is higher for wet cases than dry cases at the same value on the horizontal axis, such that the ratio of $U/U_{mf,wet}$ is the same. At $U/U_{mf,dry} = 1.1$, there are no bubbles in the wet cases, since the bed is stationary, while at $U/U_{mf,dry} = 1.3$ and 1.5, the number of bubbles is lower in the wet cases than in the dry cases, especially for the cases with high viscosity or surface tension. These results demonstrate that cohesion due to liquid bridging reduces the number of bubbles in a fluidized bed when the gas flow rate is specified. Figure 8b demonstrates that when $U/U_{mf,wet}$ is specified, the number of bubbles increases. Thus, the change in bed hydrodynamics due to adding liquid cannot be accounted for by simply using the same value of $U/U_{mf,wet}$ across wet and dry experiments.

In Figure 9, the ratio of the number of bubbles per image for cases in which silicone oil was injected to that for a dry

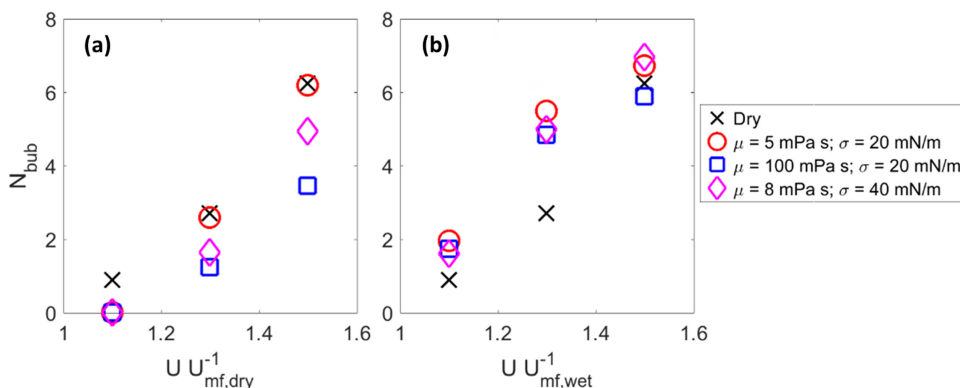


Figure 8. Average number of bubbles per frame over the entire vertical cross section of the bed vs. superficial gas velocity for various liquids for (a) varying $U/U_{mf,dry}$ and (b) varying $U/U_{mf,wet}$.

[Color figure can be viewed at wileyonlinelibrary.com]

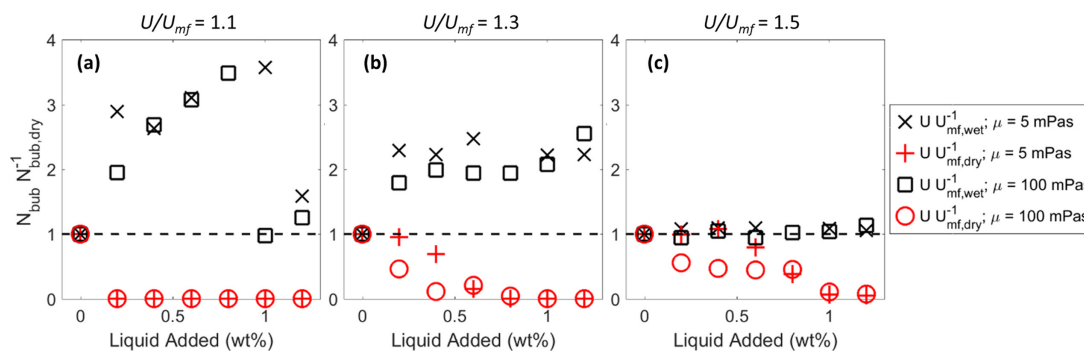


Figure 9. Ratio of average number of bubbles per frame over the entire vertical cross section of the bed to that of a dry bed vs. liquid loading of silicone oil with different viscosities at fluidizing velocities (U/U_{mf}) of (a) 1.1, (b) 1.3, and (c) 1.5.

[Color figure can be viewed at wileyonlinelibrary.com]

case is plotted vs. liquid loading for values of U/U_{mf} of (a) 1.1, (b) 1.3, and (c) 1.5. In Figure 9, red markers indicate cases in which $U/U_{mf,dry}$ is specified, and thus the same gas flow rate is used for both wet and dry cases. In contrast, black markers indicate cases in which $U/U_{mf,wet}$ is specified, and thus a higher gas flow rate is used for wet cases than dry cases. For cases in which $U/U_{mf,dry}$ is specified, the wet-to-dry ratio is always less than 1 and the ratio generally decreases with increasing liquid loading and viscosity, due to increasing cohesion preventing bubbles from forming. In some cases, the ratio is 0, indicating that no bubbles are seen in the wet case because the bed is stationary. For specified $U/U_{mf,wet}$ cases, the wet-to-dry ratio is generally greater than 1, indicating that more bubbles are seen in the wet case, especially at low gas velocities. For $U/U_{mf,wet} = 1.5$, the ratio is nearly unity for all liquid loading levels and liquid viscosities, perhaps indicating that at sufficiently high gas velocities, keeping $U/U_{mf,wet}$ constant allows for the same number of bubbles to be observed in wet and dry cases.

Figure 10 shows the average bubble diameter normalized by particle diameter vs. gas flow rate for the dry case as well as three different liquid cases, each with a liquid loading of 0.2 wt %. Figure 10a provides the results for cases in which $U/U_{mf,dry}$ is specified while (b) gives the results for cases in which $U/U_{mf,wet}$ is specified. For $U/U_{mf,dry} = 1.1$, the average bubble diameter is 0 for the wet cases, since the bed is stationary in these cases. For $U/U_{mf,dry} = 1.3$, the average bubble diameter is slightly less in the wet cases than in the dry cases,

with the bubble diameter decreasing with increasing viscosity and surface tension. For $U/U_{mf,dry} = 1.5$, the average bubble diameter is nearly identical across all wet and dry cases. At specified values of $U/U_{mf,wet}$ shown in Figure 10b, the bubble diameter in the wet cases is always slightly higher than in the dry case, demonstrating that using the same $U/U_{mf,wet}$ across wet and dry experiments is a fair approximation to keep the same bubble size, but not perfect.

Figure 11 plots the ratio of the average bubble diameter for cases in which silicone oil was injected to that for a dry case vs. liquid loading for values of U/U_{mf} of (a) 1.1, (b) 1.3, and (c) 1.5. For specified $U/U_{mf,dry}$, the wet-to-dry ratio is less than 1 for most cases and the ratio tends to decrease with increasing liquid loading and decreasing gas flow rate. Cases in which the ratio is zero indicate that there are no bubbles in the wet system and the bed is stationary. For specified $U/U_{mf,wet}$, the wet-to-dry ratio is greater than 1 but fairly close to 1, indicating that using the same value of $U/U_{mf,wet}$ is a fair but not perfect method to keep bubble size the same in moving from dry to wet fluidized beds.

The standard deviation on MRI signal (see Eq. 1) is plotted in Figure 12 vs. gas flow rate for the dry case as well as three different liquid cases, each with a liquid loading of 0.2 wt %. Wet cases at 1.1 $U/U_{mf,dry}$ all have a σ_S near 0, indicating that the bed is stationary. Wet cases at 1.3 and 1.5 $U/U_{mf,dry}$ have a non-zero value of σ_S which is lower than that of the respective dry cases, indicating that there is still bubble and particle motion, but to a lesser extent than in the dry cases due to

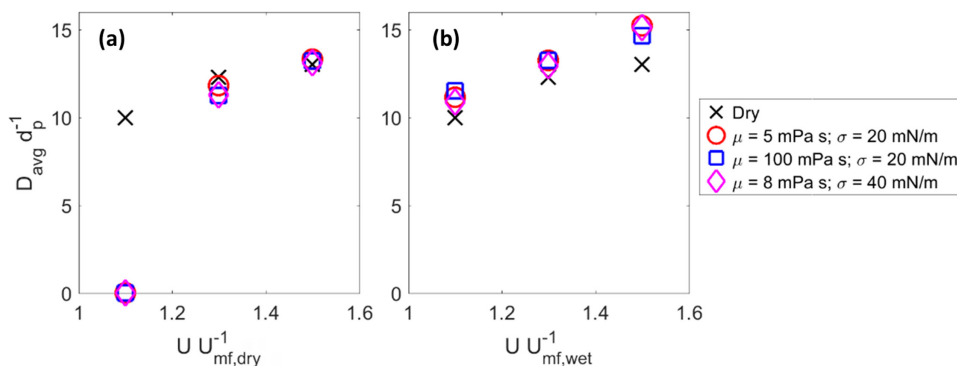


Figure 10. Average bubble diameter normalized by particle diameter averaged over the entire vertical cross section of the bed vs. superficial gas velocity for various liquids for (a) varying $U/U_{mf,dry}$ and (b) varying $U/U_{mf,wet}$.

[Color figure can be viewed at wileyonlinelibrary.com]

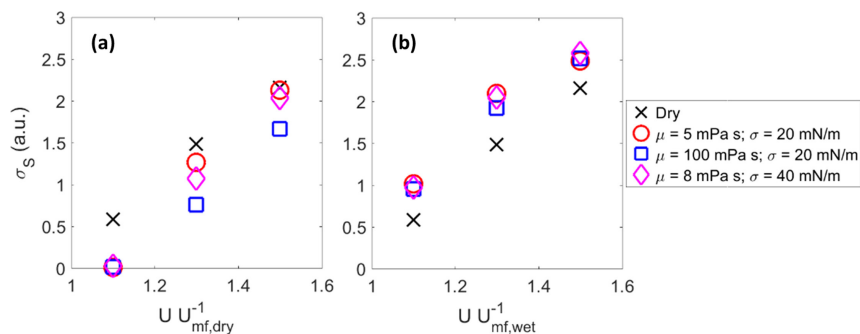


Figure 11. Ratio of average bubble diameter averaged over the entire vertical cross section of the bed to that of a dry bed vs. liquid loading of silicone oil with different viscosities at fluidizing velocities (U/U_{mf}) of (a) 1.1, (b) 1.3, and (c) 1.5.

[Color figure can be viewed at wileyonlinelibrary.com]

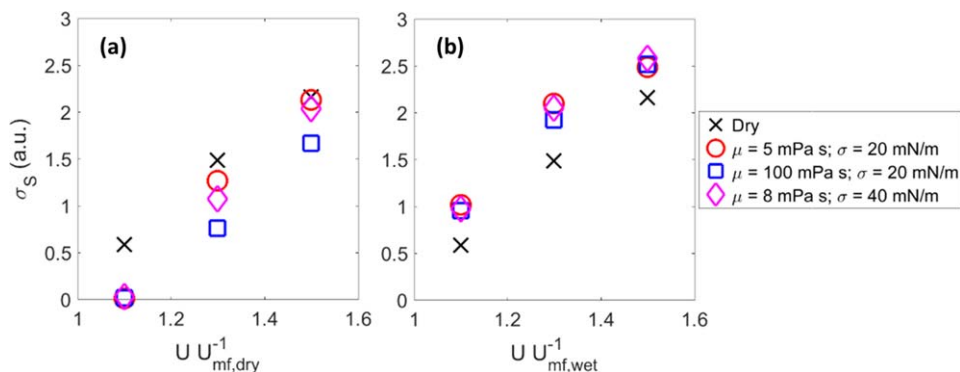


Figure 12. Standard deviation in MRI signal intensity (Eq. 1) vs. superficial gas velocity for various liquids for (a) varying $U/U_{mf,dry}$ and (b) varying $U/U_{mf,wet}$.

[Color figure can be viewed at wileyonlinelibrary.com]

interparticle forces from liquid bridges. With increasing surface tension and viscosity, σ_S decreases, indicating that stronger interparticle forces lead to less motion of bubbles and particles in the system. For specified values of $U/U_{mf,wet}$, all wet cases have similar values of σ_S which are higher than that of the respective dry cases, indicating an increased motion of bubbles and particles for wet cases than the dry cases. These results are consistent with the combined results of bubble diameter and number of bubbles in Figures 8 and 10, indicating that σ_S is an effective way to capture the extent to which a bed is vigorously fluidized.

Figure 13 shows the ratio of the standard deviation in MRI signal (see Eq. 1) for cases in which silicone oil was injected

to that for a dry case vs. liquid loading for values of U/U_{mf} of (a) 1.1, (b) 1.3, and (c) 1.5. For $U/U_{mf,dry} = 1.1$, the wet-to-dry ratios are essentially 0, indicating that all of the wet beds are stationary in this case. For $U/U_{mf,wet} = 1.1$, the wet-to-dry ratios are much greater than 1, indicating that using the same value of $U/U_{mf,wet}$ in moving from a dry to a wet system leads to a more vigorously fluidized bed at this low value of $U/U_{mf,wet}$. For $U/U_{mf,dry} = 1.3$ and 1.5, the wet-to-dry ratios steadily decrease with increasing liquid loading, indicating that increased interparticle forces from increased liquid lead to less motion of bubbles and particles in the system. For $U/U_{mf,wet} = 1.3$ and 1.5, the wet-to-dry ratios are greater than 1 and increase with liquid loading. However, the wet-to-dry

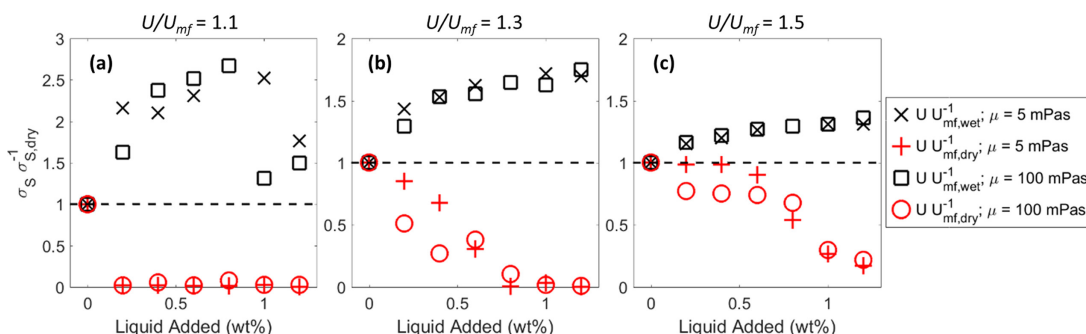


Figure 13. Ratio of standard deviation of MRI signal intensity to that of a dry bed vs. liquid loading of silicone oil with different viscosities at fluidizing velocities (U/U_{mf}) of (a) 1.1, (b) 1.3, and (c) 1.5.

[Color figure can be viewed at wileyonlinelibrary.com]

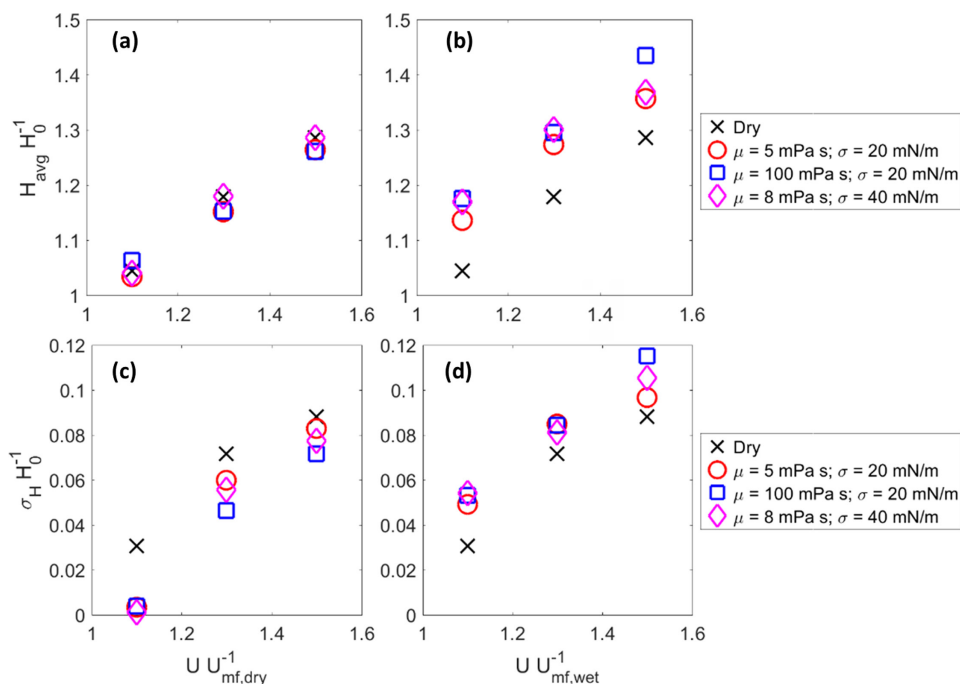


Figure 14. Average expanded bed height (first row) and standard deviation in expanded bed height (second row) normalized by dry tapped bed height (H_0) vs. superficial gas velocity for various liquids for varying $U/U_{mf,dry}$ (first column) and varying $U/U_{mf,wet}$ (second column).

[Color figure can be viewed at wileyonlinelibrary.com]

ratios are smaller for $U/U_{mf,wet} = 1.5$ than $U/U_{mf,wet} = 1.3$. These results indicate that using the same value of $U/U_{mf,wet}$ results in a more vigorously fluidized bed for wet cases than dry cases, but the approximation of producing the same hydrodynamics across wet and dry cases improves with lower liquid contents and higher fluidizing velocities.

The expanded bed height and the oscillations in the expanded bed height due to bubbling are also metrics for characterizing fluidization hydrodynamics, and thus the MR images were processed to assess bed height. The first row of Figure 14 shows the expanded bed height averaged over time for the dry case as well as wet cases with various liquids at a loading of 0.2 wt % vs. various values of (a) $U/U_{mf,dry}$ and (b) $U/U_{mf,wet}$. The average expanded bed height decreases slightly with the addition of liquid at specified $U/U_{mf,dry}$, but increases significantly with the addition of liquid at specified $U/U_{mf,wet}$. This increase in bed height when moving from dry to wet beds at the same value of $U/U_{mf,wet}$ is consistent with the results from the computational study of Boyce et al.⁵ The same plots are given in the second row of Figure 14, except for the fact that they plot the standard deviation in the expanded bed height over time as a metric of the oscillations in bed height. The standard deviation in bed height is essentially zero for wet cases at $1.1 U/U_{mf,dry}$, due to the beds being stationary, and is significantly lower than that for the dry case at higher values of $U/U_{mf,dry}$. Similar to the other indicators of bed hydrodynamics, the standard deviation in bed height is reduced the most for the very high viscosity liquid, the second most for the high surface tension liquid and the least for the low viscosity, low surface tension liquid. For constant values of $U/U_{mf,wet}$, the standard deviation in bed height increases with the addition of liquid, especially at low values of $U/U_{mf,wet}$, again showing the inaccuracy in assuming consistent bed behavior between dry and wet beds at a constant $U/U_{mf,wet}$.

To assess the behavior across varying values of liquid loading, Figure 15 shows the average (first row) and standard deviation (second row) of the expanded bed height normalized by that of a dry bed across different liquid loading levels for various gas velocities. The first row shows that the wet-to-dry ratio for average bed height does not deviate far from unity for any flow rate for either $U/U_{mf,wet}$ or $U/U_{mf,dry}$, but keeping a specified $U/U_{mf,wet}$ tends to produce a bed height which is higher than that for a dry case. The second row shows that, in contrast, the wet-to-dry ratio for standard deviation of bed height changes drastically across wetting and gas flow conditions. For $U/U_{mf,dry} = 1.1$, all of the wet beds are stationary and thus the wet-to-dry ratio is close to zero. For higher values of $U/U_{mf,dry}$, the ratio decreases from unity with increasing liquid loading, approaching zero at the highest values of liquid loading. In contrast, for constant values of $U/U_{mf,wet}$, the oscillations in bed height are greater for wet cases than dry cases and increase with liquid loading; however, the wet-to-dry ratio tends to decrease with increasing $U/U_{mf,wet}$.

In order to capture the high speeds of particles in the system, a range of velocities from -1.5 to 1.5 m/s needed to be captured using the phase-contrast measurement technique. Enabling such a wide range of velocities created noise in the data, leaving it unable to register velocities below ~ 10 cm/s with a high degree of accuracy. Since the average particle speed in some experimental cases was within this range, most notably the stationary bed cases, it was difficult to compare average particle speeds across different cases. Instead, it was more fruitful to compare particle velocity data based on the probability that a pixel had a fast-moving particle speed, outside the noise range in the measurement. Figure 16 plots the probability of a particle-laden pixel having an in-plane particle speed faster than the approximate noise range (10 cm/s) vs. gas flow rate for the dry case as well as three different liquid

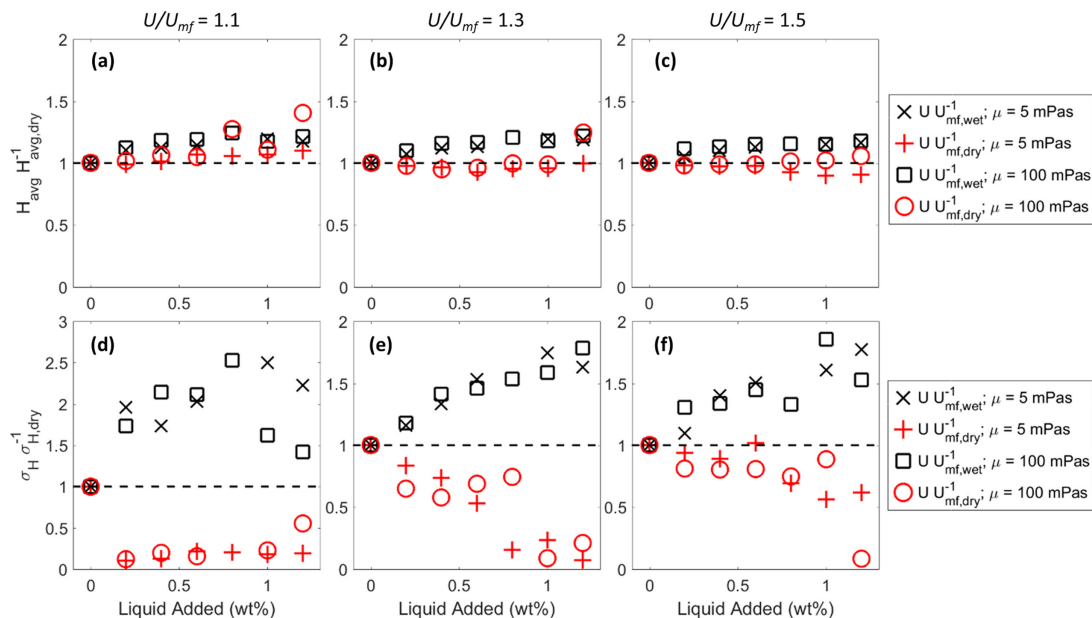


Figure 15. Ratio of the average expanded bed height (first row) and standard deviation in expanded bed height (second row) to that of a dry bed vs. liquid loading of silicone oil with different viscosities at fluidizing velocities (U/U_{mf}) of 1.1 (first column), 1.3 (second column), and 1.5 (third column).

[Color figure can be viewed at wileyonlinelibrary.com]

cases, each with a liquid loading of 0.2 wt %. Figure 16a gives the results for cases in which $U/U_{mf,dry}$ is specified while (b) shows cases in which $U/U_{mf,wet}$ is specified. The probability of particles moving at high speeds increases with increasing gas flow rate, as higher gas flow rates impart more drag on particles to move them faster in the bed. At specified $U/U_{mf,dry}$, the probability of particles moving at high speeds decreases with the addition of a liquid as well as with increasing viscosity and surface tension of the liquid, since cohesion makes it more difficult for gas to suspend the particles and for particles to move past each other quickly. The fact that the probability of particles moving was not 0 for wet cases at $U/U_{mf,dry} = 1.1$, even though the beds were stationary in these cases, indicates that this comparison is not perfect due to the noise in the measurements. For specified $U/U_{mf,wet}$, the probabilities for particles to move at fast speeds was significantly higher for the wet cases than the dry cases at low values of $U/U_{mf,wet}$ and slightly higher at high values of $U/U_{mf,wet}$. These results indicate that keeping the same value of $U/U_{mf,wet}$ is not necessarily an appropriate measure to keep particle motion constant in

moving from dry to wet cases, especially for low values of U/U_{mf} .

Figure 17 shows the ratio of the probability of particles moving at high speeds for cases in which silicone oil was injected to that for a dry case vs. liquid loading for values of U/U_{mf} of (a) 1.1, (b) 1.3, and (c) 1.5. For $U/U_{mf,wet} = 1.1$, the wet-to-dry ratio is significantly greater than 1, indicating that keeping the same value of $U/U_{mf,wet}$ is not an adequate approach to keep particle motion constant in moving from dry to wet cases close to U_{mf} . For $U/U_{mf,dry} = 1.1$, the wet-to-dry ratio is below 1, but not 0 even though the wet beds are stationary, indicating that noise in the measurements creates issues for this comparison at low U/U_{mf} . For $U/U_{mf,wet} = 1.3$, the wet-to-dry ratio is greater than 1 but significantly less than 2. For $U/U_{mf,dry} = 1.3$, the wet-to-dry ratio decreases sharply with increasing liquid loading, demonstrating that at low values of U/U_{mf} , cohesion induced by liquid bridging can keep particles from moving rapidly, often by causing the bed to channel or become stationary. For $U/U_{mf,wet} = 1.5$, the wet-to-dry ratio is slightly greater than 1 for all values of liquid

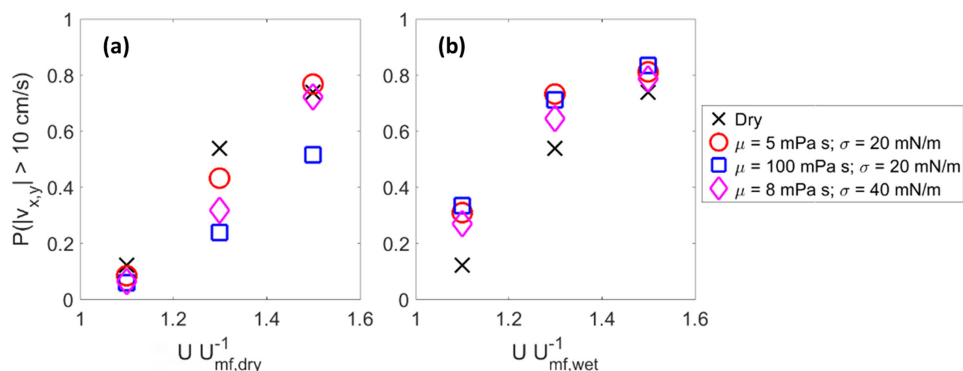


Figure 16. Probability of particle-laden pixels having an in-plane particle speed greater than 10 cm/s vs. superficial gas velocity for various liquids for (a) varying $U/U_{mf,dry}$ and (b) varying $U/U_{mf,wet}$.

[Color figure can be viewed at wileyonlinelibrary.com]

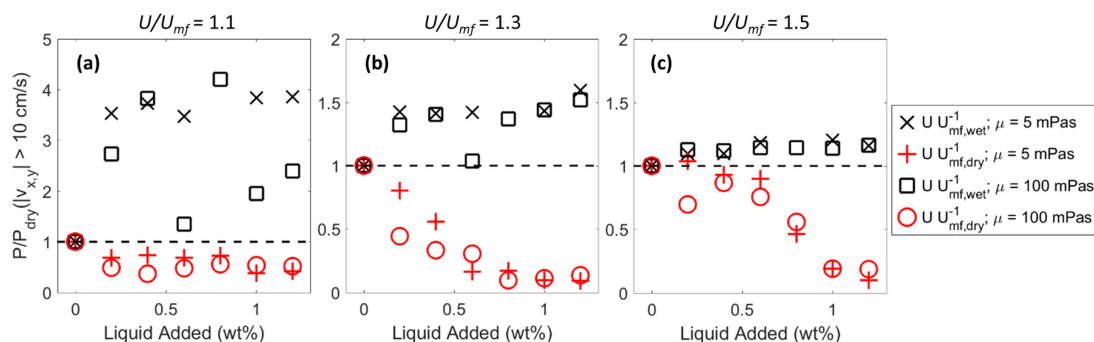


Figure 17. Ratio of the probability of particle-laden pixels having an in-plane particle speed greater than 10 cm/s to that in a dry bed vs. liquid loading of silicone oil with different viscosities at fluidizing velocities (U/U_{mf}) of (a) 1.1, (b) 1.3, and (c) 1.5.

[Color figure can be viewed at wileyonlinelibrary.com]

loading, indicating that using the same value of $U/U_{mf,wet}$ may be a good approximation for keeping the same particle motion in moving from a dry to a wet bed, if the gas flow rate is sufficiently high. For $U/U_{mf,dry} = 1.5$, the wet-to-dry ratio is less than 1 and decreases with increasing liquid loading, again indicating that cohesion from liquid bridges slows particles at constant gas flow rate.

Discussion

The results demonstrate the complementary nature of using traditional fluidization curves and state-of-the-art MRI techniques to gain unprecedented insights into the effects of liquid bridging on fluidization hydrodynamics. The results from the fluidization curves, regime map and MRI measurements of bubble dynamics, bed height and particle speed all stand to reason physically, based on the ways in which increased cohesion can affect particle packing and motion. However, the results deliver important and in some instances surprising insights into the relative effects of surface tension, viscosity, and liquid loading on hydrodynamics at various gas flow rates.

Looking across the measurements of U_{mf} , particle speed and bubble behavior, as well as the regime map, it is clear that changes between 0.2 and 1.2 wt % liquid loading are much more dominant in causing major changes in hydrodynamics than changes in surface tension by a factor of 2 or viscosity by a factor of 20. Furthermore, major changes in viscosity appear to have their largest effect at low values of liquid loading, while these changes in viscosity seem to have a negligible effect on hydrodynamics at higher values of liquid loading. At these lower values of liquid loading, the results show that changing viscosity by a factor of 20 has a more significant effect on hydrodynamics than changing surface tension by a factor of 2.

These trends present a major challenge for computational models to seek to match, based on the current trends seen in modeling studies. There is currently a debate^{5,10,33} in the literature over whether surface tension or viscous force dominates liquid bridging effects on wet granular flow, and correspondingly, whether the maximum liquid bridge force or the energy dissipated over the lifetime of a liquid bridge is most appropriate for characterizing behavior. Some models neglect the effects of surface tension or viscosity,^{10,14} while the results presented here demonstrate that changes in both result in an effect on hydrodynamics. These results should provide an important dataset for modeling studies seeking to capture the relative effects of surface tension and viscosity. Additionally,

many models for liquid bridge forces either do not account for liquid bridge volume or only account for it in such a way that has a minor effect on the bridge force,^{1,34,35} leading some studies to conclude that liquid loading is only of consequence below 0.1 wt %.^{5,14} This approach is somewhat at odds with the results found here of liquid loading dominating over surface tension and viscosity in determining bed behavior. However, liquid loading also features in models in dictating the critical separation distance for liquid bridges to rupture.³⁶ As such, liquid loading could have a relatively minor effect on the maximum bridge force, but still a significant effect on the energy dissipated over the lifetime of a bridge. Thus, the results presented here could also provide an important dataset for modeling studies seeking to understand whether modifications must be made to force models in which liquid loading only plays a minor role, or rather if energy dissipated by a liquid bridge is more important than its maximum force.

The results presented in this article also provide important insights into the validity of keeping U/U_{mf} constant across dry and wet fluidized beds to reproduce the same or comparable hydrodynamics. It is of industrial interest to find simple adjustments, such as gas flow rate, which can recreate the same hydrodynamics in wet beds needed in industry as seen in dry beds which are better understood in models and the laboratory. Thus, this question of the effect of keeping U/U_{mf} constant is important. The results here show that keeping U/U_{mf} constant is likely an overestimation of the gas flow rate necessary to produce the same hydrodynamics in a dry bed, as it produces more bubbles, larger bubbles and more fast moving particles in the wet cases as compared to the dry cases. However, there is more parity between hydrodynamic behavior between the wet and dry cases as the value of U/U_{mf} is increased, and with the values of U/U_{mf} often much greater than 1.5 used in industry, it is reasonable to view keeping U/U_{mf} constant to reproduce hydrodynamics as an appropriate approximation for industry. The trend of the effects of increasing U/U_{mf} on the accuracy of this approximation provides an important dataset for computational modeling studies to try to match. One recent computational study⁵ has noticed that similar average particle speeds are seen across dry and wet beds when U/U_{mf} is kept constant at 1.7, consistent with the experimental findings of this study. The computational study⁵ also found that at constant U/U_{mf} , the bed height increased significantly in the wet case, consistent with this study. The trends seen in the current study also motivates future tomographic imaging studies at higher values of U/U_{mf} .

It is important to describe in more detail how the current findings compare with findings from previous studies. The changes in fluidization behavior in this study with regards to increasing liquid loading, viscosity and surface tension are all consistent with a variety of previous studies, and discrepancies between studies lie largely in the extent to which each liquid aspect affects hydrodynamics. Willett³ observed using positron emission particle tracking that particle velocity decreased with increasing liquid loading, but was not significantly affected by an increase in viscosity, consistent with our results at higher liquid loading. We are unaware of prior experimental studies which have been able to investigate the effects of liquid bridging on bubble size or number of bubbles in 3D beds, pointing to the power of MRI. Previous studies^{1,2} have found discrepancies in the effect of adding liquid on the amplitude and frequency of pressure oscillations; this discrepancy can be attributed to different fluidization conditions, as well as the fact that pressure oscillations result from a variety of changes in hydrodynamics. We are unaware of any experimental studies which have investigated the validity of maintaining the same value of U/U_{mf} between wet and dry conditions, but the prior computational study of Boyce et al.⁵ produced insights consistent with those in this article. The current findings cannot resolve the debate as to whether surface tension or viscosity dominates changes in hydrodynamics,^{5,10,14} since only two values of each were used and increasing each produced a change in hydrodynamics at low values of liquid loading. Generally, we attribute discrepancies between previous experimental studies and this study to variations in the ranges of gas flow rate, liquid and particle properties studied; these discrepancies point to the need for a single study which investigates a full range of these properties. Further, any greater consistency in trends seen in this study as compared to previous studies can be attributed to the robust nature of MRI to produce detailed insights on fluidized beds without confounding aspects of wall effects in pseudo-2D beds or several competing mechanisms dictating device-scale measurements, such as pressure oscillations. Previous computational modeling studies^{1,5,14} have found a smaller effect of increasing liquid loading on fluidization hydrodynamics. This discrepancy can likely be attributed to issues or oversimplifications in sub-models for liquid transport or liquid bridge forces, and thus the results in this study provide an important benchmark for computational studies. A review article by Boyce¹⁵ provides a fuller comparison of the findings from previous studies and this study of the effects of liquid bridging on fluidization.

Conclusion

This article presents the use of MRI and fluidization curves to understand the effects of liquid bridging on fluidization hydrodynamics. Three regimes of behavior are observed: stationary, channeling and bubbling beds; this behavior is dictated largely by the gas flow rate and the amount of liquid added. The addition of liquid increases U_{mf} and U_{ff} and decreases the number of bubbles in the bed, as well as the number of fast moving particles. The results demonstrate that changes in liquid loading change behavior much more drastically than changes in the surface tension or viscosity of the liquid. Additionally, keeping U/U_{mf} constant provides reasonably similar hydrodynamics across wet and dry cases for higher values of U/U_{mf} . These general trends and the detailed quantitative findings in this article present an important benchmark against which competing theories in modeling can be tested.

Acknowledgment

This work was supported by the Swiss National Science Foundation under grant number 200021_153290.

Literature Cited

1. Mikami T, Kamiya H, Horio M. Numerical simulation of cohesive powder behavior in a fluidized bed. *Chem Eng Sci.* 1998;53(10):1927–1940.
2. Wang T, He Y, Tang T, Peng W. Experimental and numerical study on a bubbling fluidized bed with wet particles. *AIChE J.* 2016;62(6):1970–1985.
3. Willett CD. PhD Dissertation. 1999.
4. Sutkar VS, Deen NG, Patil AV, Peters EAJF, Kuipers JAM, Salikov V, Antonyuk S, Heinrich S. Experimental study of hydrodynamics and thermal behavior of a pseudo-2D spout-fluidized bed with liquid injection. *AIChE J.* 2015;61(4):1146–1159.
5. Boyce CM, Ozel A, Kolehmainen J, Sundaresan S. Analysis of the effect of small amounts of liquid on gas–solid fluidization using CFD-DEM simulations. *AIChE J.* 2017;63(12):5290–5302.
6. Seville JPK, Clift R. The effect of thin liquid layers on fluidisation characteristics. *Powder Technol.* 1984;37(1):117–129.
7. Passos ML, Mujumdar AS. Effect of cohesive forces on fluidized and spouted beds of wet particles. *Powder Technol.* 2000;110(3):222–238.
8. Geldart D. Types of gas fluidization. *Powder Technol.* 1973;7(5):285–292.
9. McLaughlin LJ, Rhodes MJ. Prediction of fluidized bed behaviour in the presence of liquid bridges. *Powder Technol.* 2001;114(1):213–223.
10. Ennis BJ, Tardos G, Pfeffer R. A microlevel-based characterization of granulation phenomena. *Powder Technol.* 1991;65(1):257–272.
11. Iveson SM, Litster JD. Growth regime map for liquid-bound granules. *AIChE J.* 1998;44(7):1510–1518.
12. Boyce CM, Ozel A, Kolehmainen J, Sundaresan S, McKnight CA, Wormsbecker M. Growth and breakup of a wet agglomerate in a dry gas–solid fluidized bed. *AIChE J.* 2017;63(7):2520–2527.
13. McDougall S, Saberian M, Briens C, Berruti F, Chan E. Effect of liquid properties on the agglomerating tendency of a wet gas–solid fluidized bed. *Powder Technol.* 2005;149(2):61–67.
14. Girardi M, Radl S, Sundaresan S. Simulating wet gas–solid fluidized beds using coarse-grid CFD-DEM. *Chem Eng Sci.* 2016;144:224–238.
15. Boyce CM. A review of gas–solid fluidization with cohesion and dissipation due to liquid bridging. Submitted. 2017.
16. Müller CR, Holland DJ, Davidson JF, Dennis JS, Gladden LF, Hayhurst AN, Mantle MD, Sederman AJ. Rapid two-dimensional imaging of bubbles and slugs in a three-dimensional, gas–solid, two-phase flow system using ultrafast magnetic resonance. *Phys Rev E.* 2007;75(2):020302(R).
17. Müller CR, Davidson JF, Dennis JS, Fennell PS, Gladden LF, Hayhurst AN, Mantle MD, Rees AC, Sederman AJ. Real-time measurement of bubbling phenomena in a three-dimensional gas–fluidized bed using ultrafast magnetic resonance imaging. *Phys Rev Lett.* 2006;96(15):154504.
18. Boyce CM, Rice NP, Ozel A, Davidson JF, Sederman AJ, Gladden LF, Sundaresan S, Dennis JS, Holland DJ. Magnetic resonance characterization of coupled gas and particle dynamics in a bubbling fluidized bed. *Phys Rev Fluids.* 2016;1(7):074201.
19. Penn A, Tsuji T, Brunner DO, Boyce CM, Pruessmann KP, Müller CR. Real-time probing of granular dynamics with magnetic resonance. *Sci Adv.* 2017;3(9):e1701879.
20. Müller CR, Holland DJ, Sederman AJ, Scott SA, Dennis JS, Gladden LF. Granular temperature: comparison of magnetic resonance measurements with discrete element model simulations. *Powder Technol.* 2008;184(2):241–253.
21. Fabich HT, Sederman AJ, Holland DJ. Study of bubble dynamics in gas–solid fluidized beds using ultrashort echo time (UTE) magnetic resonance imaging (MRI). *Chem Eng Sci.* 2017;172:476–486.
22. Pavlin T, Wang R, McGorty R, Rosen MS, Cory DG, Candela D, Mair RW, Walsworth RL. Noninvasive measurements of gas exchange in a three-dimensional fluidized bed by hyperpolarized ¹²⁹Xe NMR. *Appl Magn Reson.* 2007;32(1–2):93–112.
23. Boyce CM, Rice NP, Sederman AJ, Dennis JS, Holland DJ. 11-Interval PFG pulse sequence for improved measurement of fast velocities of fluids with high diffusivity in systems with short T2*. *J Magn Reson.* 2016;265:67–76.

24. Boyce CM, Rice NP, Davidson JF, Sederman AJ, Dennis JS, Holland DJ. Magnetic resonance imaging of gas dynamics in the freeboard of fixed beds and bubbling fluidized beds. *Chem Eng Sci.* 2016;147:13–20.
25. Washburn EW. The dynamics of capillary flow. *Phys Rev.* 1921; 17(3):273–283.
26. Yuan Y, Lee TR. Contact angle and wetting properties. In: *Surface Science Techniques. Springer Series in Surface Sciences.* Berlin: Springer, 2013:3–34.
27. Stehling MK, Turner R, Mansfield P. Echo-planar imaging: magnetic resonance imaging in a fraction of a second. *Sci Wash.* 1991; 254(5028):43.
28. Nyquist H. Certain topics in telegraph transmission theory. *Trans Am Inst Electr Eng.* 1928;47(2):617–644.
29. Pruessmann KP, Weiger M, Scheidegger MB, Boesiger P. SENSE: sensitivity encoding for fast MRI. *Magn Reson Med.* 1999;42(5):952–962.
30. Caprihan A, Fukushima E. Flow measurements by NMR. *Phys Rep.* 1990;198(4):195–235.
31. Fukushima E. Nuclear magnetic resonance as a tool to study flow. *Annu Rev Fluid Mech.* 1999;31(1):95–123.
32. Toomey RD, Johnstone HF. Gaseous fluidization of solid particles. *Chem Eng Prog.* 1952;48(5):220–226.
33. Pont V, Saleh K, Steinmetz D, Hémati M. Influence of the physico-chemical properties on the growth of solid particles by granulation in fluidized bed. *Powder Technol.* 2001;120(1):97–104.
34. Willett CD, Adams MJ, Johnson SA, Seville JPK. Capillary bridges between two spherical bodies. *Langmuir.* 2000;16(24):9396–9405.
35. Pitois O, Moucheront P, Chateau X. Liquid bridge between two moving spheres: an experimental study of viscosity effects. *J Colloid Interface Sci.* 2000;231(1):26–31.
36. Lian G, Thornton C, Adams MJ. A theoretical study of the liquid bridge forces between two rigid spherical bodies. *J Colloid Interface Sci.* 1993;161(1):138–147.

Manuscript received Aug. 31, 2017, and revision received Nov. 14, 2017.